

# Assessment of Infrasound Detectors Based on Analyst Review, Environmental Effects, and Detection Characteristics

by Junghyun Park, Chris T. Hayward, Cleat P. Zeiler,  
Stephen J. Arrowsmith, and Brian W. Stump

**Abstract** To assess infrasound detector performance, automated detections by the progressive multichannel correlation method (Cansi, 1995) and the adaptive  $F$ -detector (AFD; Arrowsmith *et al.*, 2009) are compared with signals identified by five independent analysts. Each detector was applied to a 4-hr time sequence recorded by the Korean seismoacoustic array, CHNAR, composed of small ( $< 100$  m) and large ( $\sim 1000$  m) aperture subarrays. Detector effectiveness was estimated for a selection of array elements and detection thresholds under low- and high-noise conditions. Estimated receiver operating characteristic based on events identified by analysts evaluates the change in detection probability ( $P_d$ ) and false-alarm probability ( $P_f$ ) for various detector parameters. This empirical study documents that the use of smaller aperture subarrays by both detectors increases  $P_d$  with smaller  $p$ -values recommended for AFD to minimize  $P_f$ .  $P_d$  is impacted most by noise level, as shown by an increase in detections for average root mean square amplitudes from 1.2 to 3.2 MPa. Critical to this assessment is the identification of the source of the noise, constrained by signal characteristics, complementary seismic observations, and realistic atmospheric modeling. Based on signal characteristics (correlation value, phase velocity, and detection azimuth) and raytracing using global and local weather datasets, we conclude that during low-noise conditions some detections from local distances (10–50 km) are affected by surface wind direction, and a second set is affected by tropospheric winds. This illustrates the role that surface and higher-atmosphere winds play in array performance when assessing signals from regional infrasound sources in which local detections may be considered as noise or clutter.

**Electronic Supplement:** Figures showing summary of detection results and polar plots of correlation estimates and phase velocity with respect to azimuth.

## Introduction

Renewed interest in infrasound has stemmed from the use of acoustic arrays in the nuclear test, International Monitoring System (IMS), which ultimately will include 60 globally distributed infrasonic arrays (Christie and Campus, 2010). With the addition of various research infrasound efforts, in total there are about 100 continuously operating infrasound arrays worldwide (Hedlin *et al.*, 2012). The increasing density of infrasound stations provides regional coverage in some areas, that is, USAArray Transportable Array (Vernon *et al.*, 2012). These dense networks record signals from many small near-surface sources including earthquakes, volcanic eruptions, and mining explosions on both seismic and infrasonic sensors (Hagerty *et al.*, 1999). Studies that combine seismic and infrasound signals signifi-

cantly improve source identification and constrain propagation path effects.

As is true of automatic seismic detectors, automated infrasound detectors reduce analyst workload and streamline the detection process, the first step in source location and ultimately source characterization. The need to identify in excess of 1000 events per month at a single array (Evers and Haak, 2001; Matza *et al.*, 2013) has prompted the development of several automated infrasound detectors including the progressive multichannel correlation (PMCC) algorithm (Cansi, 1995), InfraTool (Hart, 2004), and the adaptive  $F$ -detector (AFD) (Arrowsmith *et al.*, 2009). Because infrasound signals that propagate to regional and global distances are strongly influenced by time-varying propagation effects,

automatic detectors use a waveform correlation among individual array elements, rather than high-fidelity template matching as is possible for seismic signal detection. In this work, two detectors, AFD and PMCC, are explored.

PMCC assumes that the noise is uncorrelated between any two sensor elements and applies progressive processing to the data recorded by different array elements by first assessing cross-correlation functions of subarrays and then adding additional array elements to reduce false alarms (Cansi, 1995). The method simultaneously estimates trace velocity and azimuth.

InfraTool (Hart, 2004) applies the Hough transform, first proposed by Brown *et al.* (2002), to calculate azimuth, trace velocity, and correlation coefficient using moving multiple overlapping windows for coherent signal identification. InfraTool uses a least-square solution to compute the trace velocity, minimizing the residual from the observations, and declares a signal when detections meet a set of detection criteria. Brown *et al.* (2008) applied the automatic detection based on the Hough transform to data from IMS infrasound arrays.

To assess the optimum detector, Blandford (1974, 2002) tested the performance of a detector based on the conventional *F*-statistic, focusing on the impact of array aperture, distance range, frequency band, and correlation of signals from nuclear explosions. Garcés and Hetzer (2002) document that this approach performs well when values of correlation and an associated *F*-statistic are high. AFD (Arrowsmith *et al.*, 2009) adaptively modifies the conventional *F*-statistic based on time-varying empirical estimates of the background noise, producing a time-adaptive *F*-statistic. Similar to detection of seismic phases (Zeiler and Velasco, 2009), an important additional criterion for these tools is a basis for association of multiple detections to estimate event location.

Detection methods have been evaluated in terms of receiver operating characteristic (ROC) curves (Kay, 1998) that quantify the relationship between detection and false-alarm probabilities as a function of detection threshold. The challenge in analyzing ROC curves lies in developing a realistic-labeled dataset for which the signals are known and span the space of possible signal characteristics, while also including noise that spans the space of possible noise characteristics. An effort to develop such a dataset for regional and global infrasound monitoring is currently underway at Commissariat à l'Energie Atomique, Sandia National Laboratories, Los Alamos National Laboratory, Southern Methodist University (SMU), Korea Institute of Geoscience and Mineral Resources (KIGAM), and International Data Centre. The development of a pseudosynthetic dataset using synthetic signals and real noise can be thought of as a compromise between purely synthetic datasets (the standard for ROC curve analyses), in which there is total control over the labels (signals and noise), and real datasets, in which the labels are not truly known and must be estimated by analysts. The problem in building synthetic datasets is in realistically duplicating characteristics of the signals and noises, to the

extent that an analyst, using daily processing techniques, would be unable to recognize that the dataset is synthetic. Without such fidelity in synthetic datasets, detector comparisons based on such data are suspect. However, in the absence of true data with ground truth (referred to above as labeled data), it is important to provide a protocol to compare detectors.

Based on this argument, an alternate approach to the estimation of ROC curves is to use real data and signals identified by analysts. To assess the performance of automated detectors in the absence of ground truth, we determine the estimated receiver operating characteristic (EROC) using events identified by multiple analysts from the same dataset, following procedures implemented in several seismic observation studies. Freedman (1966) first studied estimates of picking errors from analyst-reviewed seismograms using nine analysts and researchers. Sereno (1990) and Leonard (2000) assessed automatic picks comparing results with those produced by analysts and quantified the misclassification of seismic phases, mistiming of seismic phases, and poor-phase association (Sipkin *et al.*, 2000). Zeiler and Velasco (2009) focused on measurements by highly experienced analysts at a number of institutions. They concluded that the primary contributing factors to analysts' pick errors are ambient noise levels, distance from source to receiver, magnitude, source mechanisms, and propagation effects. We take this approach one additional step using characteristics of the infrasound detections, analysis of complementary seismic observations, and raytracing using realistic atmospheric conditions to refine the identification of the sources of the signals in this study.

In this pilot study, we compare two automated infrasound detectors with a manually reviewed time sequence of data to estimate the EROC. The test procedure using PMCC and AFD was to apply varying detection parameters (detection threshold and array configuration) to the same dataset, a 4-hr sequence of infrasound data at the Korean infrasound array CHNAR. The results of the automated procedures are compared with picks by five independent analysts of varying experience as a step toward assessing the effectiveness of these procedures in terms of changing environmental conditions during the time period of the dataset. We document the detection results (correlation value, phase velocity, and detection azimuth) estimated from the automated detectors and analysts, and analyze the source characteristics by raytracing using global and local weather datasets. Finally, the effect of surface weather conditions on background noise and detection performance is quantified.

## Detectors

Detection of infrasound signals typically consists of processing stages that include preprocessing (filtering and time-windowing data), estimation (estimation of the direction of arrival), hypothesis testing (determining the statistical significance of a particular feature), and postprocessing (determining which detections in different time-frequency cells are related). PMCC and AFD use different approaches for

Table 1  
Detection Processing Parameters

| Parameters                                  | Automatic Detectors                            |   |
|---|--|---|
|   | AFD  | PMCC                                    |
| <b>Detection</b>                            |  |   |
| Filter band (Hz)                            | 1–5  |   |
| Time window (s)                             | 20   |   |
| Overlap (%)                                 | 50   |   |
| <i>p</i> -value                             | 0.001, 0.005, 0.01, 0.03, 0.05, 0.07, and 0.09 | —                                       |
| Adaptive window (hr)                        | 1  | —                                       |
| Consistency (s)                             | —  | 0.01, 0.05, 0.1, 0.3, 0.5, 0.7, and 0.9 |
| <b>Family</b>                               |  |   |
| Standard deviation for azimuth (°)          | —  | 10                                      |
| Standard deviation for phase velocity (m/s) | —  | 20                                      |
| Phase velocity range (m/s)                  | —  | 250–450                                 |

Detection processing parameters used in the tests of automatic detectors, adaptive *F*-detector (AFD) and progressive multichannel correlation (PMCC).

each step. For example, each approach uses a different time-frequency discretization as well as different strategies to handle clutter (continuous or repetitive signals). AFD uses broadband processing and updates the noise distribution based on clutter, whereas PMCC uses narrowband processing to separate signal and clutter on the basis of spectral characteristics. We compare the entire processing sequence of each detector (preprocessing, estimation, and hypothesis testing), as implemented in the software releases of InfraMonitor and WinPMCC.

#### Adaptive F-Detector

AFD (Arrowsmith *et al.*, 2009) incorporated in Infra-Monitor employs the *F*-statistic with a null hypothesis of perfectly uncorrelated noise (Blandford, 2002) that is time dependent. Automatic detection is based on the *F*-statistic defined as

$$F = \frac{\left( \frac{J-1}{J} \right)}{\times \frac{\sum_{n=n_0}^{n_0+(N-1)} \left[ \sum_{j=1}^J x_j(n+l_j) \right]^2}{\sum_{n=n_0}^{n_0+(N-1)} \left( \sum_{j=1}^J \left\{ x_j(n+l_j) - \left[ \frac{1}{J} \sum_{m=1}^J x_m(n+l_m) \right] \right\}^2 \right)}}, \quad (1)$$

in which *J* is the number of sensors,  $x_j(n)$  is the waveform amplitude of the *n*th sample of the time series with the mean removed from sensor *j*,  $l_j$  is the time-alignment lag based on beamforming,  $n_0$  is the starting sample number for processing, and *N* is the number of samples in the processing window. The *F*-statistic is based on a *p*-value, the probability of obtaining an *F*-statistic at least as extreme as the calculated value under the *F*-distribution:  $p\{F(t)\}$ , from all elements in an array for each time window.

The theoretical *F*-statistic in the presence of correlated noise is distributed as

$$C \times F_{2BT,2BT(J-1)}, \quad (2)$$

in which *B* is the bandwidth of the filtered data, *T* is the length of the processing window, *J* is the number of sensors, and *C* is the factor aligning the peaks of the observed and theoretical *F*-distributions as defined by

$$C = \left( 1 + J \frac{P_s}{P_n} \right). \quad (3)$$

$P_s/P_n$  denotes the signal-to-noise ratio (SNR; Shumway *et al.*, 1999), the ratio of the correlated noise power to uncorrelated noise power (Arrowsmith *et al.*, 2008).

To capture changes in noise with time, the standard *F*-detector is modified with estimates of *C* for the adaptive windows. The observed distribution of the *F*-statistic ( $F_{2BT,2BT(J-1)}$ ), estimated from the output of a frequency-wavenumber (*f*–*k*) analysis (Rost and Thomas, 2002) and original input parameters, is adapted to the theoretical *F*-distribution ( $C \times F_{2BT,2BT(J-1)}$ ) by estimating the maximum *C*-value. The remapped *F*-statistic can be used with a standard *p*-value threshold to declare a detection with a specified statistical significance. Processing parameters used in the detection tests are summarized in Table 1. Further exploration of these parameters and their relationship to time-dependent environmental conditions can be found in Park (2013).

#### Progressive Multichannel Correlation

PMCC (Cansi, 1995) assumes uncorrelated noise, resulting in detections in the presence of clutter (or correlated noise), which must be removed via postprocessing. It is based on progressive processing of data recorded by subarrays of a larger array using time-domain cross-correlation estimates between individual stations (Cansi, 1995). The first step in PMCC uses cross correlation to measure the time delay  $\Delta t_{ij}$  between all pairs of signals,  $S_i(t)$  and  $S_j(t)$  at stations *i* and *j*, in each three-element subarray. In the case of a

wave propagating without distortion, the delay is frequency independent

$$\Delta t_{ij} = \frac{1}{2\pi f} (\varphi_j(f) - \varphi_i(f)), \quad (4)$$

(Cansi and Le Pichon, 2009), in which  $\varphi_i(f)$  and  $\varphi_j(f)$  represent the phases at stations  $i$  and  $j$ , respectively. For a plane-wave signal observed at three sensors, the sum of time delays between the stations obeys a closure relation, which is used as a phase detector

$$\Delta t_{ij} + \Delta t_{jk} + \Delta t_{ki} = 0. \quad (5)$$

The second PMCC step is progressive (Cansi and Le Pichon, 2009) in which the consistency of the set of delays is estimated with all sensors ( $n$ ) in a subnetwork  $R_n$  and defined as the mean quadratic residual of the closure relations

$$R_n \ni i, j, k \left\{ \begin{array}{l} r_{ijk} = \Delta t_{ij} + \Delta t_{jk} + \Delta t_{ki} \\ C_n = \sqrt{\frac{6}{n(n-1)(n-2)} \sum_{i>j>k} r_{ijk}^2} \end{array} \right. \quad (6)$$

(Cansi and Le Pichon, 2009). When the consistency  $C_n$  is below a threshold, a detection is declared on  $R_n$ . The network aperture is progressively increased to provide the most robust estimates of signal phase velocity and azimuth using the maximum number of sensors. Hereafter, to avoid confusion between consistency ( $C_n$ ) and  $C$ -value from equation (3), we will call it the consistency value.

Testing of these detectors is focused on regional infrasound arrays with signals from 1 to 5 Hz typically associated with small natural and man-made events. Tuning parameters were based on the PMCC testing of Garcés and Hetzer (2002) as well as on experience with AFD documented in the next section of the article. One difference in PMCC, mentioned earlier, is that detections are assessed in the time domain using a band-pass filter. Each frequency band within each time window represents a pixel of data, which is analyzed independently, followed by comparison with adjacent pixels in time and frequency to group the nearest-neighbor pixels with similar characteristics into families (Garcés and Hetzer, 2002). Detection parameters including family settings used for the tests are summarized in Table 1. The distribution of back azimuths as well as phase velocities observed varies with season and depends on the specific infrasonic arrival, but in this study these effects are not investigated. Incorporation of this type of information will require an iterative procedure linked to phase identification coupled to the analysis of a broader set of data covering longer time periods.

## Data and Analysis

A 4-hr dataset (02:00:00–06:00:00 in UTC, 11 a.m. to 3 p.m. in local time, 2 January 2012) recorded by the seismoacoustic array CHNAR is used in this analysis. The 4-hr time sequence was chosen for the number of easily identified

signals as well as a transition from low to higher wind noise conditions halfway through the time period. Previous studies (Stump *et al.*, 2004; McKenna *et al.*, 2008) document large numbers of seismoacoustic events observed at CHNAR for similar time periods and suggest that the sources are man-made.

The CHNAR array consists of a small 100-m aperture infrasound array embedded in a larger 1-km aperture array (Fig. 1). Each station in the larger array includes one additional infrasound sensor ~50 m from the main element. A total of 10 infrasound microphones (Chaparral Physics Model 2.0 microphones) and 4 seismometers (GS-13, located at large aperture sites) make up the array that is sampled at 40 samples/s. The center element has a weather station measuring wind velocity, wind azimuth, and temperature, at 2 m above the surface and sampled once per second. Each microphone is attached to 10 porous hoses, 8 m in length connected at the center for reducing background noise. Data are recorded on 24-bit digitizers (Geotech DR24) and sent in real time to KIGAM in South Korea and to SMU in Texas.

Characteristics of seismic and seismoacoustic (infrasound arrivals associated with an observed seismic signal) events recorded at CHNAR have been discussed in several studies. The detectable infrasound signals at CHNAR that have been linked to man-made sources such as quarry blasts, airport construction, military exercises, and chemical plant explosions were identified based on seismoacoustic analysis (Che *et al.*, 2002; Stump *et al.*, 2004). However, the majority of observed detections are from lonesome infrasound signals (i.e., unassociated infrasound signals; McKenna *et al.*, 2008). These lonesome infrasound signals, which are independent of ground truth and contain information about unknown sources, have been used to assess infrasound propagation in the fine-scaled lower atmosphere (McKenna *et al.*, 2008). This study will use these same approaches to analyze both lonesome infrasound signals and seismoacoustic events recorded at CHNAR, to assess detector performance. We note that seismic and infrasound signals during the time period of the data used in this study may be associated with man-made sources near the array.

Filtered (1–5 Hz) infrasound and seismic waveforms are displayed in Figure 2, with four easily identified large infrasound signals near 03:00:00 UTC from the southeast and south based on initial PMCC output (see Fig. S1, available in the electronic supplement to this article). Two seismic signals are associated with directions from 135° and 170° during this time period, suggesting that these sources are generating both seismic and acoustic signals (Fig. 2). The time differences between seismic and infrasound arrivals are consistent with a source distance from CHNAR within 100 km, similar to previous studies at the site (Che *et al.*, 2002; Stump *et al.*, 2004; McKenna *et al.*, 2008). Based on the seismic  $S-P$  times (1.5 and 4.0 s) of the two seismic signals, distance estimates of the sources from CHNAR are ~12 and ~35 km. There are no directly associated infrasound arrivals with these seismic signals, but several infrasound signals correlated with

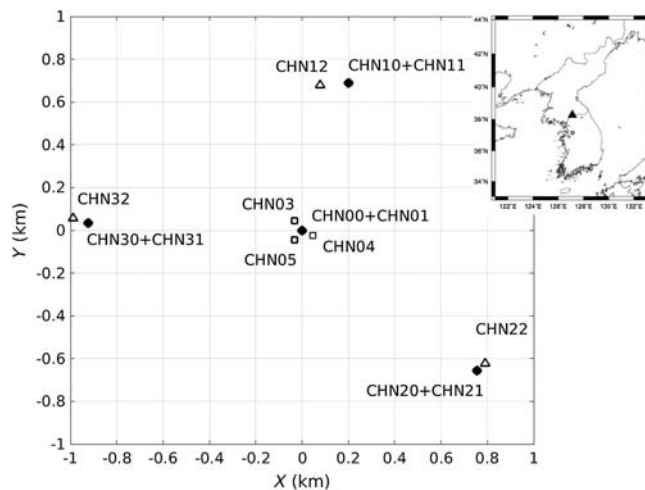


**Figure 1.** The relative configuration of CHNAR array elements and absolute location map (triangle in the inset map). The four elements in the 1-km aperture seismoacoustic array, CHN00/10/20/30 (circles) each have a GS-13 seismometer (CHN01/11/21/31) and an infrasound gauge (Chaparral Physics Model 2.0). These instruments are supplemented by the small aperture (< 100 m) infrasound subarray, CHN00/03/04/05 (squares) deployed around the center element. Additionally, each of three outer sites has an additional infrasound gauge, CHN12/22/32 (triangles), offset by about 50 m from the primary. The location of Osan meteorological observatory is depicted as an open circle in the inset map.

the seismic source directions are observed following the seismic arrivals.

The 4-hr infrasound dataset has noise levels that increase after the first two hours, producing two data segments with different background noise levels. The first two hours of data were recorded under wind velocities near 0 m/s, and the second two hours had an average wind velocity up to 3 m/s (Fig. 3a). AFD remaps the  $F$ -distribution in time to account for these time-varying noise conditions using the  $C$ -value (equation 3). A 1-hr adaptive window was used during the AFD processing based on a detector tuning study of Park (2013).  $C$ -value changes in time estimated for the different array configurations are compared with 5-min averages of wind velocity and azimuth at the site (Fig. 3a). Estimates based on all array elements for the first two hours of data have relatively high  $C$ -values (1.5–2.7) associated with low wind velocities from the east (first hour) and south (second hour), whereas the last two hours of data have smaller  $C$ -values of 1.1–1.8, with higher wind velocities and azimuths from the northwest (Fig. 3a). In the large aperture estimates, the  $C$ -values are not as variable in time as for the small aperture estimates, which may reflect decreased signal correlation under low-noise conditions for the large aperture array consistent with local noise sources. The variation of  $C$ -values is larger for the smaller array aperture estimates, indicating higher sensitivity between noise level and coherence on the small aperture array elements. In all cases, the  $C$ -value is dependent on weather conditions, especially wind speed. This result is consistent with the parameter tuning

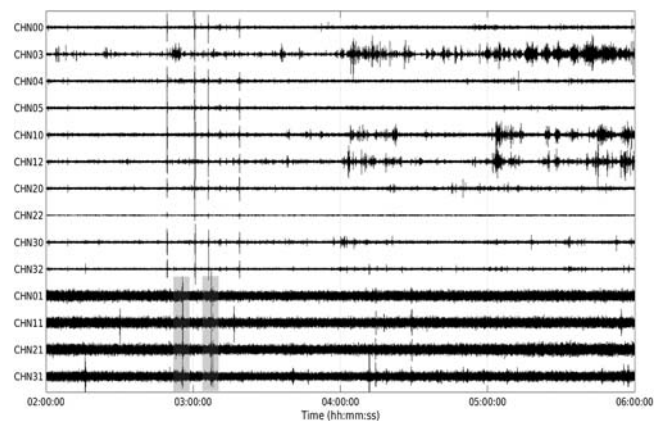


**Figure 2.** The 4-hr infrasound (upper 10 traces) and seismic (lower 4 traces) datasets (02:00:00–06:00:00 in UTC, 11 a.m. to 3 p.m. in local time, 2 January 2012) recorded at the seismoacoustic array CHNAR. Waveforms were filtered from 1 to 5 Hz. Two seismic arrivals that have source directions from 135° and 170°, respectively, are highlighted in gray boxes.

study in the Korean Peninsula (Park *et al.*, 2016) that documents a decrease in the  $C$ -value with increasing wind velocity for a number of arrays.

The two detectors were tested using four different starting configurations or subnetworks, as summarized in Table 2. As noted previously, one difference between PMCC and AFD is the use of subnetworks. AFD uses all array elements in a given configuration (small, large, small + large, and all array elements). PMCC automatically assigns subnetwork configurations based on a user-defined configuration. Because each subnetwork has a total of three elements, a three-sensor threshold is applied. To document the use of different subnetworks on PMCC processing, large aperture arrays using a consistency of 0.1 s were tested with all array elements together (single subnetwork of 00/10/20/30) and with multiple subnetworks (00/10/20 + 00/10/30 + 00/20/30 + 10/20/30) (see Fig. S1). The number of detections using all array elements together is smaller than that using the subnetwork combinations. Detections with smaller consistency values were observed during the first two hours of data, whereas few detections meeting the consistency constraints are found in the last two hours of data when background noise levels are higher. Detections using all array elements together are found to produce conservative results (low detection numbers, especially in the last two hours of the dataset; Park, 2013). The assessment of detection performance and array configurations will be further discussed in the Analyst Review section.

The numbers of automatic detections are dependent on background noise levels as well as algorithmic tuning parameters. Both detectors were tested with different values of consistency for PMCC and  $p$ -values for AFD (Table 1) and different combinations of array elements (Table 2). The numbers of detections from these tests are summarized in Figure 4a. Both detectors are strongly dependent on threshold

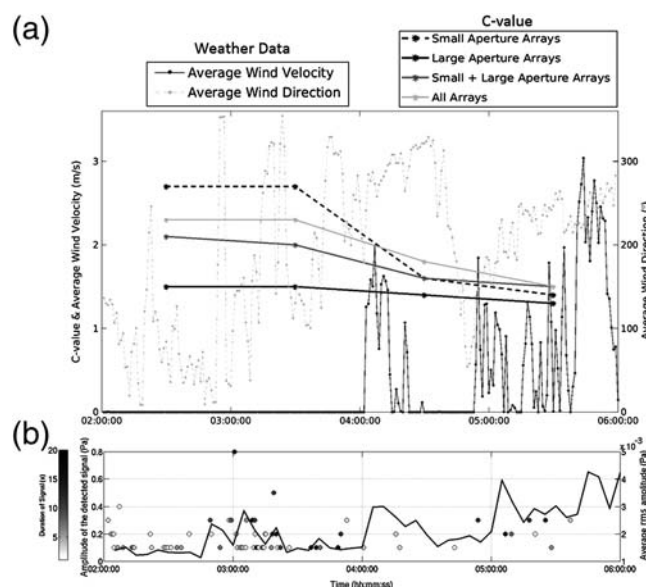


**Figure 3.** (a)  $C$ -values (left  $y$  axis) estimated by adaptive  $F$ -detector (AFD) using different array configurations are plotted as a function of time and compared with wind velocity (left  $y$  axis) and direction (right  $y$  axis) based on 5-min averages from the CHNAR data (02:00:00–06:00:00 in UTC, 2 January 2012). (b) The average root mean square (rms) amplitude (black line) as a function of time is estimated using all waveforms and is compared with the amplitude (left  $y$  axis) and duration (left bar) of the detected signals identified by analyst 5.

values of  $p$ -value and consistent with higher threshold values producing larger numbers of detections. For AFD, higher  $p$ -values produce larger numbers of detections based on the  $F$ -distribution and may include correlated noise. Test results for PMCC show that the number of detections increases as the consistency value is increased up to 0.3 s, illustrating the effect of small timing differences between arrivals on individual array elements. Both detectors produce a smaller number of detections when the large aperture arrays are used, with about 30% of the number of detections produced using the small aperture arrays. Larger consistency values for PMCC produce a greater number of automated detections at the expense of signal quality across the array consistent with the acceptance of larger timing discrepancies between array

elements. Detections produced by PMCC are more dependent on the array configuration with many detections in the case of small aperture arrays.

### Analyst Review

Five analysts individually reviewed the 4-hr dataset. Their results are used to assess the automated detectors, providing a basis for optimizing their application. Each analyst was free to define unique criteria for event identification. Based on individual interpretations of the data, the frequency band of filtering applied by each analyst was slightly different (i.e., 1–5 Hz for analysts 1, 2, and 5; 0.5–4.0 Hz for analyst 3; and 4.0–8.0 Hz for analyst 5). The experience level of the analysts varied, three were labeled as experts based on a long history of signal analysis and two as new and undergoing training. All of these used time-domain and  $f$ – $k$  analysis tools in GEOTool (Coyne and Henson, 1995) to identify signals. The number of detections produced by each analyst is compared with the output of the automatic detectors (Fig. 4b) and summarized in Table 3. The number of detections identified by analysts (average number 77) is higher than those determined by either automated detector (average number of 48 for AFD and 60 for PMCC). AFD and PMCC each used a 20-s time window with 50% overlap, and therefore multiple phases within this time window can only be separately identified by the analysts. Signal arrival times estimated by analysts were cataloged in a manner similar to the automated detectors to effectively compare the two by evenly dividing the 4-hr dataset into consecutive 20-s windows, with each window evaluated for signal detections. Figure 5 displays the windows with signal detections identified by the five analysts and automatic detections for each of the 20-s time windows. Analysts and automatic detections are consistent during the first 2-hr data window (Fig. 5). During the last two hours of data, in which the noise levels are higher, there are fewer automated PMCC detections, although AFD has a large number of detections. During this high-noise data, detections by analysts were substantially reduced. This result highlights that detection under higher background noise conditions is difficult for both automatic systems and humans.

**Table 2**  
Configurations of CHNAR Used in This Study

| Configurations | Aperture Size   | Arrays Used for Test   |
|----------------|---|--|
| AFD (S)        | A small aperture (< 100 m) array                            | 00/03/04/05  |
| PMCC (S)       |   | Subnetworks: 00/03/04 + 00/04/05 + 00/03/05 + 03/04/05                       |
| AFD (L)        | A large aperture (~1 km) array                              | 00/10/20/30  |
| PMCC (L)       |   | Subnetworks: 00/10/20 + 00/10/30 + 00/20/30 + 10/20/30                       |
| AFD (S + L)    | A hybrid of small and large aperture arrays                 | 00/03/04/05/10/20/30   |
| PMCC (S + L)   |   | Subnetworks: 00/03/04 + 03/04/05 + 00/20/30 + 10/20/30                       |
| AFD (All)      | A combination of small, large, and sublarge aperture arrays | CHN00/03/04/05/10/20/30/12/22/32   |
| PMCC (All)     |   | Subnetworks: 00/03/04 + 03/04/05 + 00/20/30 + 10/20/30 + 00/12/22 + 12/22/32 |

Four different CHNAR array configurations used for testing of PMCC and AFD. S, small; L, large.

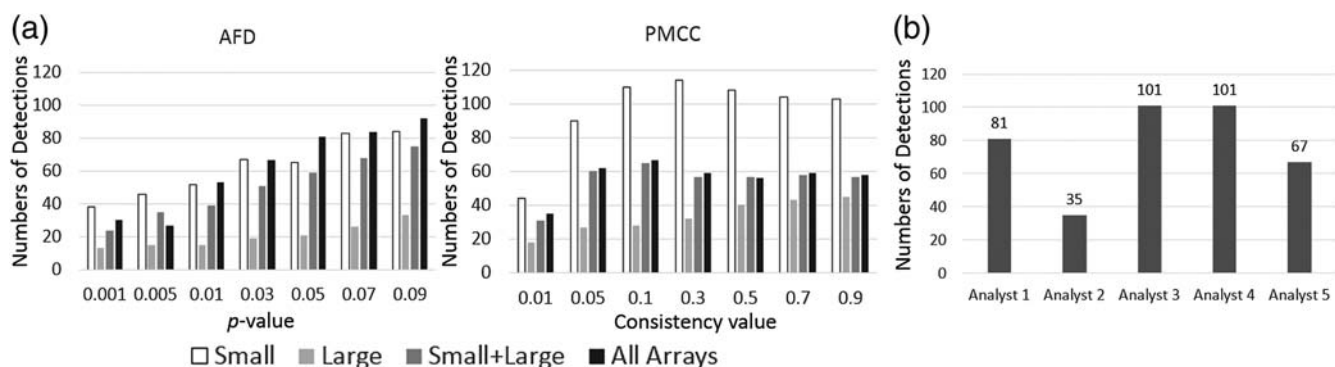


**Figure 4.** Comparison of the total number of (a) automatic picks as a function of array configuration and threshold values ( $p$ -value and consistency value) and (b) manual picks from the five analysts for the 4-hr block of infrasound data recorded at CHNAR. PMCC, progressive multichannel correlation.

### EROC Curves

Basic processing tools were used by the analysts in this study, realizing that they frequently use automatic tools such as PMCC and AFD in manually adapted iterative-processing workflows, and the role of human analyst and automatic processor can be blurred. ROC curves are used to quantify detection and false-alarm probabilities (Johnson and Dudgeon, 1993), providing a basis for detector optimization. This approach has been used to assess the performance of adaptive and conventional detectors such as AFD, as noted by Arrowsmith *et al.* (2009). ROC curves estimate the trade-off between the detection probability ( $P_d$ ) and the false-alarm probability ( $P_f$ ) for a range of detection thresholds as defined by

$$P_d = \frac{\text{Number of detected signals}}{\text{Total number of signals}} \quad (7)$$

**Table 3**  
The Number of Detections Estimated by AFD and PMCC

| Automatic Detectors | Threshold Values | Array Configurations  |                       |                                 |            |
|---------------------|------------------|-----------------------|-----------------------|---------------------------------|------------|
|                     |                  | Small Aperture Arrays | Large Aperture Arrays | Small and Large Aperture Arrays | All Arrays |
| AFD                 | 0.001            | 38                    | 13                    | 24                              | 30         |
|                     | 0.005            | 46                    | 15                    | 35                              | 27         |
|                     | 0.01             | 52                    | 15                    | 39                              | 53         |
|                     | 0.03             | 67                    | 19                    | 51                              | 67         |
|                     | 0.05             | 65                    | 21                    | 59                              | 81         |
|                     | 0.07             | 83                    | 26                    | 68                              | 84         |
|                     | 0.09             | 84                    | 33                    | 75                              | 92         |
|                     | 0.1              | 44                    | 18                    | 31                              | 35         |
|                     | 0.3              | 110                   | 28                    | 65                              | 67         |
| PMCC                | 0.05             | 90                    | 27                    | 60                              | 62         |
|                     | 0.1              | 114                   | 32                    | 57                              | 59         |
|                     | 0.3              | 114                   | 32                    | 57                              | 59         |
|                     | 0.5              | 108                   | 40                    | 57                              | 56         |
|                     | 0.7              | 104                   | 43                    | 58                              | 59         |
|                     | 0.9              | 103                   | 45                    | 57                              | 58         |

The number of detections estimated by AFD and PMCC using the four different starting configurations (Table 2) with different detection thresholds ( $p$ -values for AFD and consistency values for PMCC).

$$P_f = \frac{\text{Number of noise detections}}{\text{Total number of detection intervals during noise}}. \quad (8)$$

ROC analysis can be accomplished by inserting known signals of varying size into realistic noise to provide a known number of signals within a dataset. As an alternative, a modified data-centric procedure is introduced that compares the output of automated detectors with detections identified by analysts. The total number of signals is defined by the analyst in this application and is therefore an alternative performance assessment in the absence of ground truth. In this application, results from the five analysts using individual signal-detection criteria were utilized, although detections were not always consistent across all analysts. Therefore, more than two common readings from the five analysts were set as the reference for the ROC (Fig. 5a). To distinguish this comparison from the traditional approach, these curves are called EROCs.

Equations (7) and (8) were applied to 720 consecutive 20-s time windows (Fig. 5) using the definition of reference events from the analysts' review to estimate  $P_d$  and  $P_f$ . The EROC analysis explores the effect of different threshold values ( $p$ -value and consistency value) and array configurations while dividing the data into the first 2-hr block (low wind and noise) and the last 2-hr block (higher wind and noise) (Fig. 6). Depending on the reference values that are used to estimate the EROC, the curves change as a function of time, because the analysts identify a smaller number of signals under the higher noise conditions.

During the first two hours of data, the two automated detectors produce similar detection trends with  $P_d$  increasing as  $P_f$  increases (Fig. 6a). The performance of each detector depends on array configuration and threshold values ( $p$ -value and consistency value). PMCC produces the highest  $P_d$  ( $\sim 0.62$ ), although the maximum  $P_d$  for AFD ( $\sim 0.59$ ) is similar. In the case of PMCC, the largest  $P_d$  ( $\sim 0.62$ ) is accompanied by the largest  $P_f$  ( $\sim 0.25$ ) using the small aperture configuration. AFD produces the largest  $P_d$  ( $\sim 0.59$ ) with a  $P_f$  of  $\sim 0.16$  using all array elements. The smallest  $P_d$  ( $\sim 0.24$ ) and  $P_f$  ( $\sim 0.01$ ) for PMCC occurs using the large aperture array. Similarly, the smallest  $P_d$  ( $\sim 0.21$ ) with  $P_f$

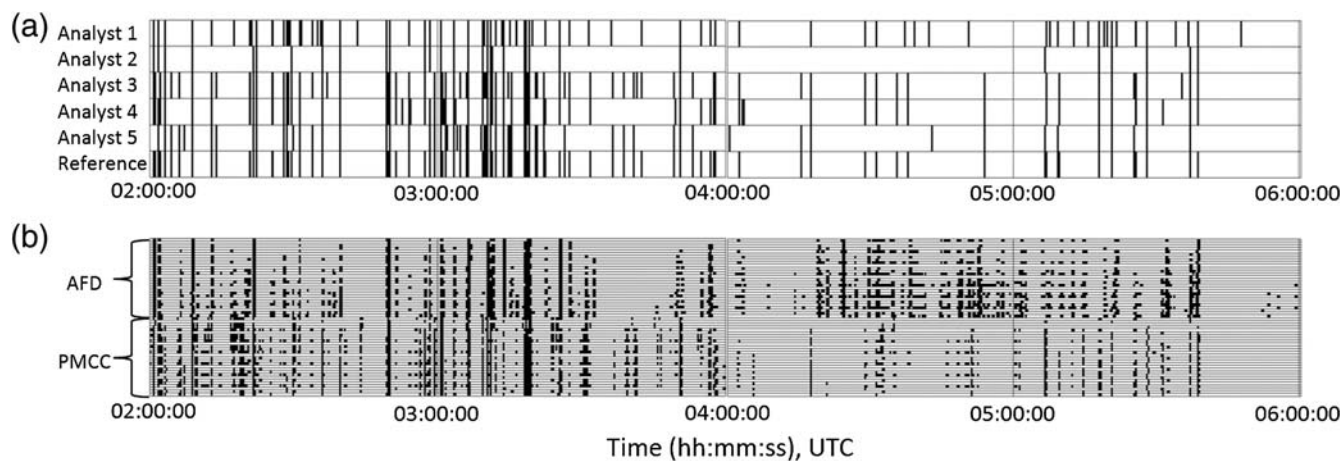


**Figure 5.** Detection times estimated by (a) five analysts and (b) the automatic detectors for each 20-s time window. AFD includes all detection times for different configurations and different  $p$ -values (0.001, 0.005, 0.01, 0.03, 0.05, 0.07, and 0.09; from top to bottom). PMCC includes all detection times for different configurations and different consistency values (0.01, 0.05, 0.1, 0.3, 0.5, 0.7, and 0.9; from top to bottom).

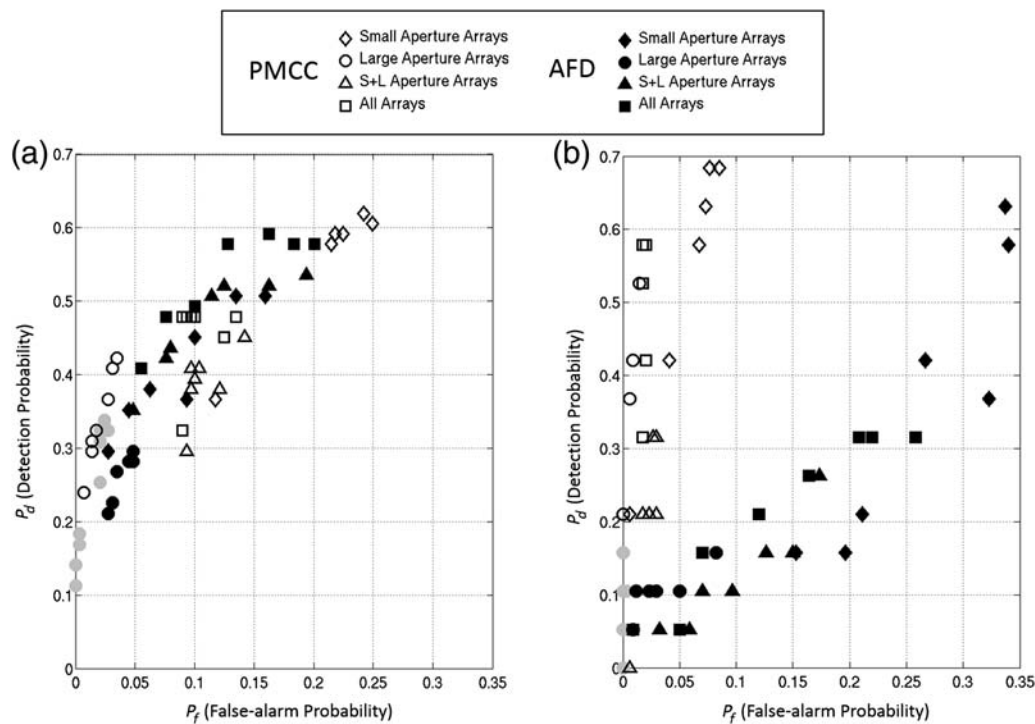


**Figure 6.** The estimated receiver operating characteristic (EROC) for the automatic detectors using different aperture arrays and different threshold values for (a) the first 2 hrs and (b) the second 2 hrs of data. Gray circles indicate the detection and false-alarm probability from detections using PMCC with conservative single subnetwork based on Park (2013) (Table 4). An expanded version focusing on the effects of threshold values and array configurations is shown in Figure 7.

(~0.03) for AFD occurs using the large aperture array. Park (2013) documents detection performance for different aperture arrays using a single subnetwork (configuration is summarized in Table 4). This result shows relatively lower estimates of  $P_d$  with small  $P_f$  (gray circles, Fig. 6).

Under high-noise conditions, the performances of the two automatic detectors are significantly different (Fig. 6b). Both detectors produce a broad range of  $P_d$  (0.20–0.69 for PMCC

and 0.05–0.65 for AFD), whereas PMCC has a narrower range of  $P_f$  (0.01–0.08) than AFD (0.01–0.34). The use of small aperture arrays in PMCC produces the highest  $P_d$  (~0.69). AFD also produces the highest  $P_d$  (~0.64) using the small aperture array, but  $P_f$  is much larger (0.34). Both detectors produce higher  $P_d$  values using small aperture arrays under high-noise condition. Automated processing using small aperture arrays detected more of the signals that analysts

Table 4  
Configurations of Single Subnetwork(s) Used in Park (2013)

| Aperture Size   | Arrays Used for Test                              |
|---|---|
| A small aperture (<100 m) array                             | Subnetwork: 00/03/04/05                           |
| A large aperture (~1 km) array                              | Subnetwork: 00/10/20/30                           |
| A hybrid of small and large aperture arrays                 | Subnetworks: 00/03/04/05 + 00/10/20/30            |
| A combination of small, large, and sublarge aperture arrays | Subnetworks: 00/03/04/05 + 00/10/20/30 + 12/22/32 |

Four different starting CHNAR array configurations for PMCC tested in Park (2013). The results are shown in Figure 6.

picked compared with estimates using other array configurations.

Based on the tests using different array configurations and threshold values, both detectors using smaller threshold values produce the smallest values of  $P_d$  and  $P_f$  (Fig. 7). Under low-noise condition,  $P_d$  and  $P_f$  for PMCC do not vary much with consistency value, except for the case that uses only data from the large aperture (Fig. 7a). In contrast, AFD produces a relatively narrow range of  $P_d$  and  $P_f$  using the large aperture array. When using the small and large aperture arrays or all array elements,  $P_d$  values from AFD for all  $p$ -values are larger than those from PMCC. There was no  $C$ -value variation with time for the large aperture array (Fig. 3a), whereas this configuration shows the poorest detection performance (Fig. 7). Under high-noise conditions, there is not much difference between the performance using small threshold values (i.e.,  $p$ -value of 0.001 and consistency value of 0.01 s) for PMCC and AFD (Fig. 7b). At higher threshold values, PMCC and AFD perform quite differently, with higher  $P_d$  and lower  $P_f$  for PMCC and lower  $P_d$  and higher  $P_f$  for AFD. These results illustrate how detections estimated by the two automatic detectors are linked to the initial assumption (correlated noise or signal). PMCC is based on the cross correlation between signals recorded at subarrays, and AFD depends on the mapping of the observed  $F$ -distribution to the theoretical distribution accounting for time variations in background noise.

PMCC produces results that are most similar to those of the analysts, with the largest  $P_d$  for the smallest consistency value. AFD in contrast classifies some of the signals as correlated noise under an assumed  $p$ -value, especially under high-noise conditions. AFD has the best detection performance using the small aperture array, but  $P_f$  is increased, suggesting that the smaller  $p$ -value might be recommended. During high-noise conditions, analysts reported difficulty in identifying signals, suggesting that a number of signals might have gone undetected or that some of the detections represented coherent noise across the array. The dependence of the EROC results on the analysts' picks illustrates an intrinsic shortcoming of this empirical assessment procedure and motivates exploration of datasets with complementary ground-truth information.

### Interpretation of Detections

We compare detection parameters (correlation value, phase velocity, and detection azimuth) from the automatic

detectors and analysts. These parameters along with raytracing using global and local weather datasets are used to assess the sources of the detections in the absence of ground-truth information. The impact of surface weather conditions on the detection process is also investigated. The root mean square (rms) amplitude and frequency content of the detected signals and background noise levels are used to constrain the sources of the signals to separate true infrasound arrivals from clutter including local noise sources.

The azimuthal distributions of detections are concentrated from 90° to 210° and from 240° to 330° over the 4-hr time period. The sources of these detection clusters may be local signals associated with human activities. Stump *et al.* (2004) document that many of the seismoacoustic signals from the southeast to southwest have a single source region including mining or construction sites, and detections from the northwest might be related with natural seismicity. Che *et al.* (2002) also note that many seismoacoustic events are from the southeast to southwest within 200 km of CHNAR and related to human activities identified as quarries, mines, industrial, or military sites. The majority of infrasound observations in this work are also correlated with these directions, consistent with these man-made activities. Two seismic arrivals associated with directions of 135° and 170° were observed during the first two hours (Fig. 2), suggesting sources that generate both seismic and infrasound signals, possibly mining or other types of explosions at local distances (Che *et al.*, 2002). The distance estimates based on seismic  $S-P$  times are 12 and 35 km, respectively, close to the array. Correlation estimates with respect to azimuth for both automatic detectors are compared (Fig. 8a) with values from AFD relatively larger (0.4–1.0) than those from PMCC (0.2–0.8). Both AFD and PMCC detection clusters during the first two hours have high correlations that match the azimuths of the two seismic detections, with a bias of ~5° between the two estimates, possibly introduced by atmospheric winds. During the last two hours of data, the automatic detection estimates are generally more scattered, although in the case of human detections there is a cluster from ~300° to 330°, consistent with the direction of the prevailing tropospheric winds during this time period. This result suggests that the infrasound signals from 90° to 210° possibly were stopped, were masked by the noise during the second two hours, or the environmental conditions are such that propagation to the station is impeded. This observation is consistent with a change in direction of near-surface winds measured at the array in which the surface

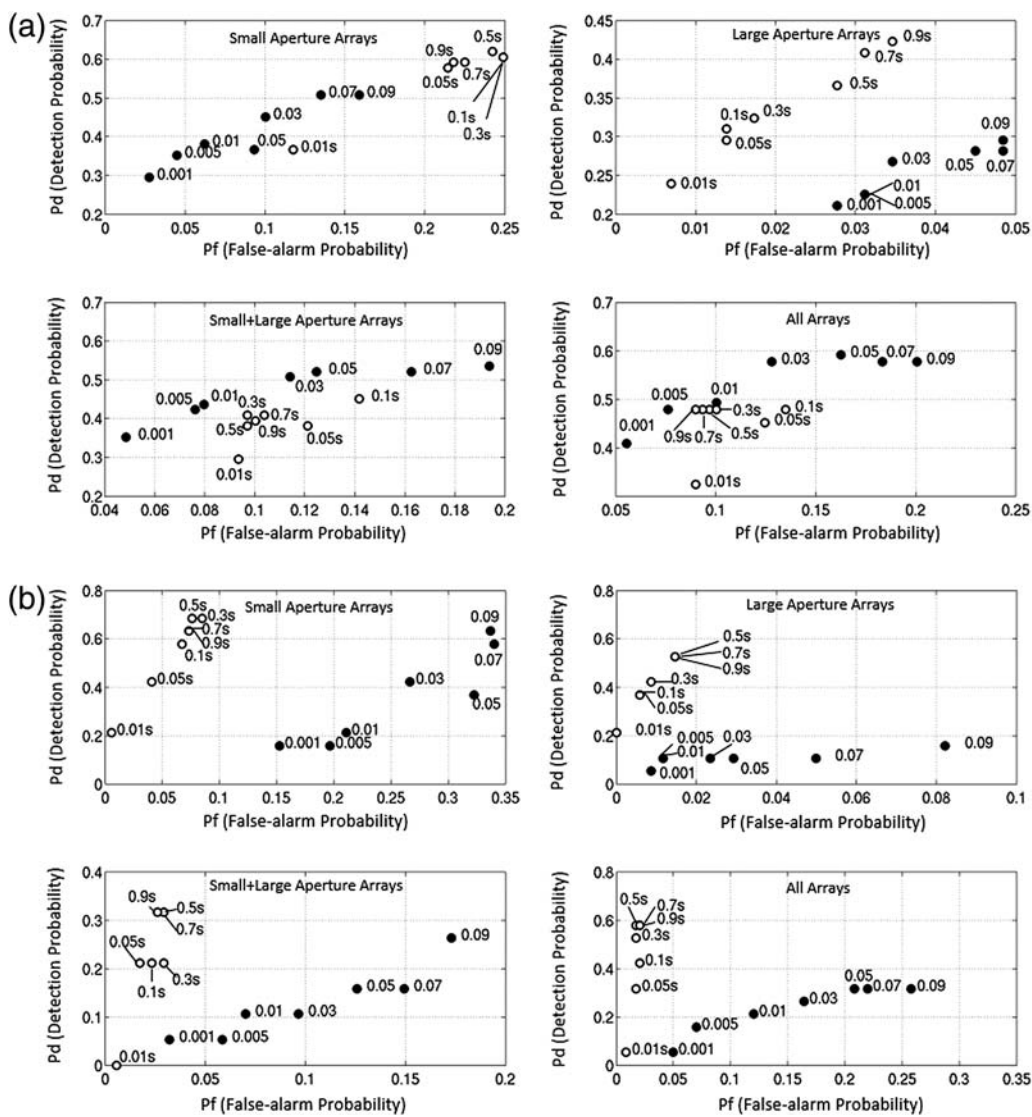


**Figure 7.** The EROC for the automatic detectors using (a) the first 2 hrs and (b) the last 2 hrs of data documenting the effects of different aperture arrays and threshold values. AFD (black circles) includes  $p$ -values of 0.001, 0.005, 0.01, 0.03, 0.05, 0.07, and 0.09. PMCC (white circles) includes consistency values of 0.01, 0.05, 0.1, 0.3, 0.5, 0.7, and 0.9 s.

wind direction is from the east (first hour), south (second hour), and west-northwest (last two hours) (Fig. 3a). The frequency content of the signals during the first two hours is relatively high and broad from 1 to 5 Hz (Fig. S1). These comparisons suggest that local signals are propagated from the east and south as a result of the fine details in the near-surface atmosphere, including the surface winds and a possible wintertime inversion layer near the array during the analysis time period (11 a.m. to 1 p.m.). The frequency content of signals for the last two hours is more narrowband (3–5 or 1–3 Hz) (Fig. S1), suggesting a more distant source from the northwest with energy that has decayed with distance. There were no seismic observations associated with the infrasound detections for the last two hours. Detailed polar plots of detections, including the effects of threshold value and array configuration, are shown in Figure S2.

Infrasound phase identification depends on estimates of both phase velocity and celerity. Without ground-truth information that includes source location in space and time, the estimation of celerity is not possible. Phase velocity can help constrain the propagation path because its value depends on the velocity at the turning height of the infrasound energy that returns to the surface (McKenna *et al.*, 2008). Phase velocities estimated by the analysts and automatic detectors are relatively fast, ranging from 320 to 350 m/s (Fig. 8b). AFD produced a few phase velocity estimates below 200 m/s for the last two hours of data, indicating that these detections might not be infrasonic arrivals. Seasonal variations of phase velocity estimates have been reported in the literature, with lower estimates during the winter than those for the summer (McKenna *et al.*, 2008; Park *et al.*, 2016). Signals identified in these previous studies were

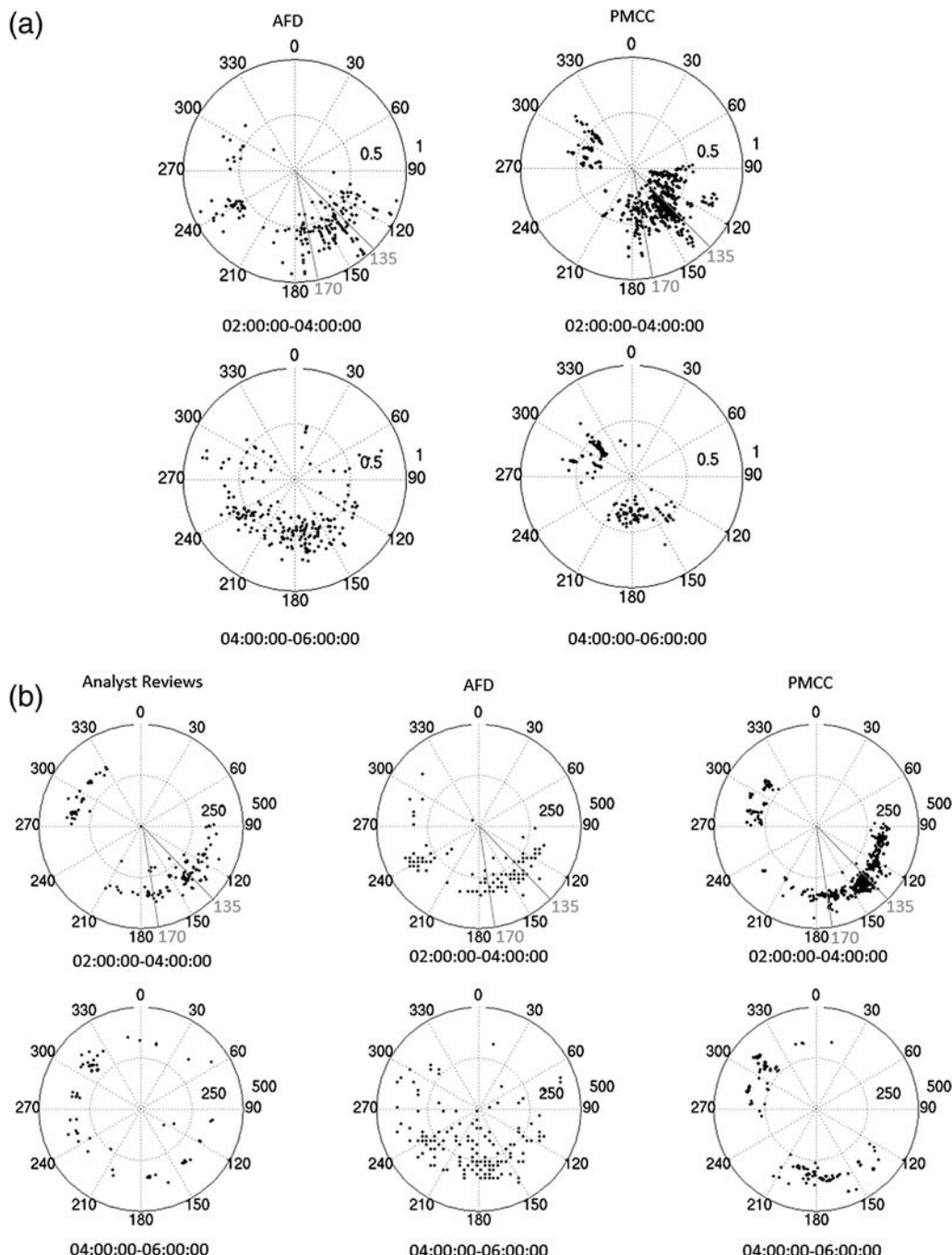


**Figure 8.** Polar plots of (a) correlation estimate and (b) phase velocity (m/s) with respect to azimuth based on both analyst reviews and automatic detectors for the first 2 hrs (top) and the last 2 hrs (bottom). Two dominant seismic-source directions of 135° and 170° that may be associated with infrasound signals during the first two hours are plotted as gray lines. Detailed polar plots as a function of threshold values and array configurations are displayed in [Figure S2](#) (available in the electronic supplement to this article).

argued to be a result of local propagation and attributed to tropospheric arrivals and thus affected by lower atmospheric temperatures and winds during the winter.

To explore the predicted characteristics of infrasound propagation near CHNAR during the time period of our tests, 3D raytracing (Blom and Waxler, 2012) was conducted using global and local weather data. Six-hour Ground-to-Space (G2S) atmospheric specifications (Drob *et al.*, 2003) at

CHNAR (00 and 06 UTC) were used. Local meteorological (LM) observations from Osan, South Korea (Fig. 1), for the same time period (00 and 06 UTC) were also utilized. Even though this observatory is ~100 km from CHNAR, the LM velocity profile to a height of 30 km was used to assess tropospheric propagation in previous studies (Che *et al.*, 2002; Stump *et al.*, 2004; McKenna *et al.*, 2008). These two velocity profiles of zonal and meridional winds are similar (Fig. 9),

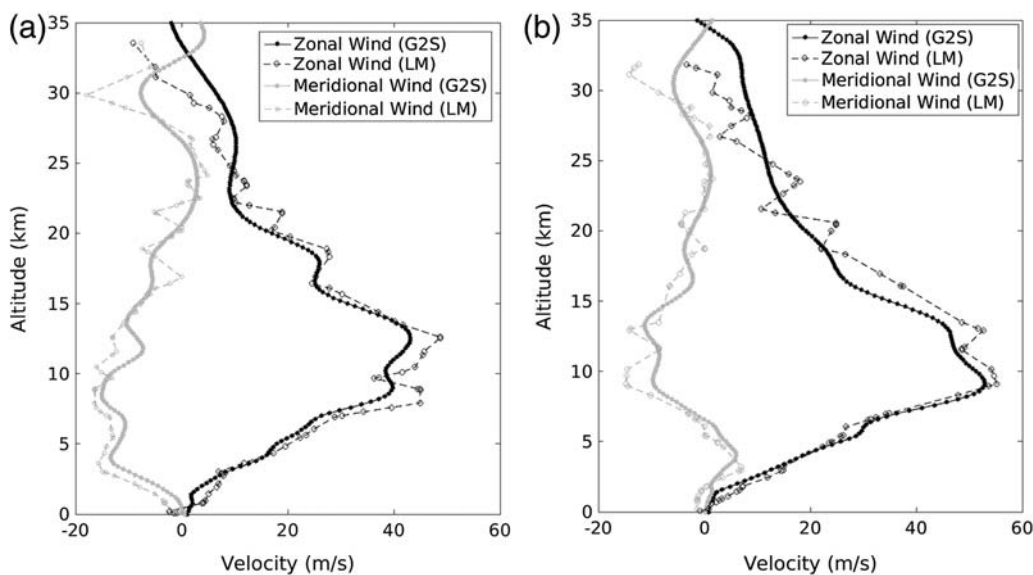


**Figure 9.** Comparison of zonal and meridional wind speeds from Ground-to-Space (G2S) specifications above the CHNAR site and local meteorological (LM) observatory in Osan for 2 January 2012 at (a) 00:00:00 and (b) 06:00:00 UTC.

because G2S atmospheric specifications are based on the well-resolved and constrained operational meteorological analysis fields from the National Oceanic and Atmospheric Administration Global Forecast System analysis fields below 35 km (Kalnay *et al.*, 1990) with high spatial sampling (altitude spacing of 0.2 km). Both profiles document high wind speeds from 8 to 15 km, whereas the LM profile has relatively higher speeds than the G2S at lower altitudes for 00 UTC. Raytracing was conducted using inclination angles from 0.5° to 60.5°, with a step of 1°, a maximum number of surface bounces of 10, and a source elevation of 0.2 km based on Cartesian coordinates.

Figure 10 compares raytracing results through the tropospheric models using the G2S and LM data at 00 and 06 UTC. High wind velocities from the west and northwest produce a strong tropospheric ensonified region from 0° to 270° at 00 UTC and from 0° to 150° at 06 UTC. Detections from 300° to 330° in this study might be associated with this dominant wind, consistent with tropospheric arrivals predicted by raytracing. These results do not explain the preponderance of detections from the east to the southeast. As already discussed, surface wind might be responsible for arrivals along very close-in paths, with surface winds dominantly from the east for the first hour and from the south for the second hour (Fig. 3a). These local sources illuminated by surface weather conditions might be considered clutter to the problem of detecting and locating regional sources of infrasound. Surface winds are from the west for the last two hours (Fig. 3a), consistent with the direction of tropospheric ducting predicted by both G2S and LM data, suggesting that sources during this time may be a combination of local and near regional.

The average rms amplitude of the waveforms increases with wind velocity (Fig. 3). To assess the impact of increasing wind velocity on detection, the average rms amplitude

and average wind velocity during consecutive 5-min windows for the complete dataset were computed. Waveforms used in the analysis were filtered from 1 to 5 Hz, consistent with the frequency band of interest. The average time-dependent rms amplitudes  $AA_{rms}$  were calculated using the filtered waveforms from all array elements:

$$AA_{rms} = \sqrt{\frac{\sum_{i=1}^T \left\{ (\sum_{j=1}^N A^2)/N \right\}}{\Delta T}}, \quad (9)$$

in which  $A$  is the amplitude of waveform at a particular sample,  $N$  is the number of infrasound array elements,  $T$  is the time window, and  $\Delta T$  is the total time duration. These estimates are compared with the average wind velocity estimates in Figure 3b documenting the strong correlation between rms amplitude and wind velocity during the 4-hr time period. Average rms noise amplitudes varied from 1.2 to 4.5 MPa. The amplitude and duration of the detected signals identified by analyst 5 are also displayed in Figure 3b, illustrating that relatively small amplitude signals were detected under low-noise conditions, whereas the number of small amplitude detections is significantly reduced during periods of higher background noise. Similarly,  $P_d$  values from the automatic detectors and analysts' results are impacted by noise level, with low noise (average rms amplitude of 1.7 MPa) having an average  $P_d$  of ~0.42 and an average  $P_f$  of ~0.10 and high noise (average rms amplitude of 2.9 MPa) having an average  $P_d$  of ~0.30 with an average  $P_f$  of 0.08.

The number of detections produced by the automatic detectors and the analysts was counted and compared against the rms amplitude and wind speed, based on the 5-min windows (Fig. 11a). Generally, the number of automatic and

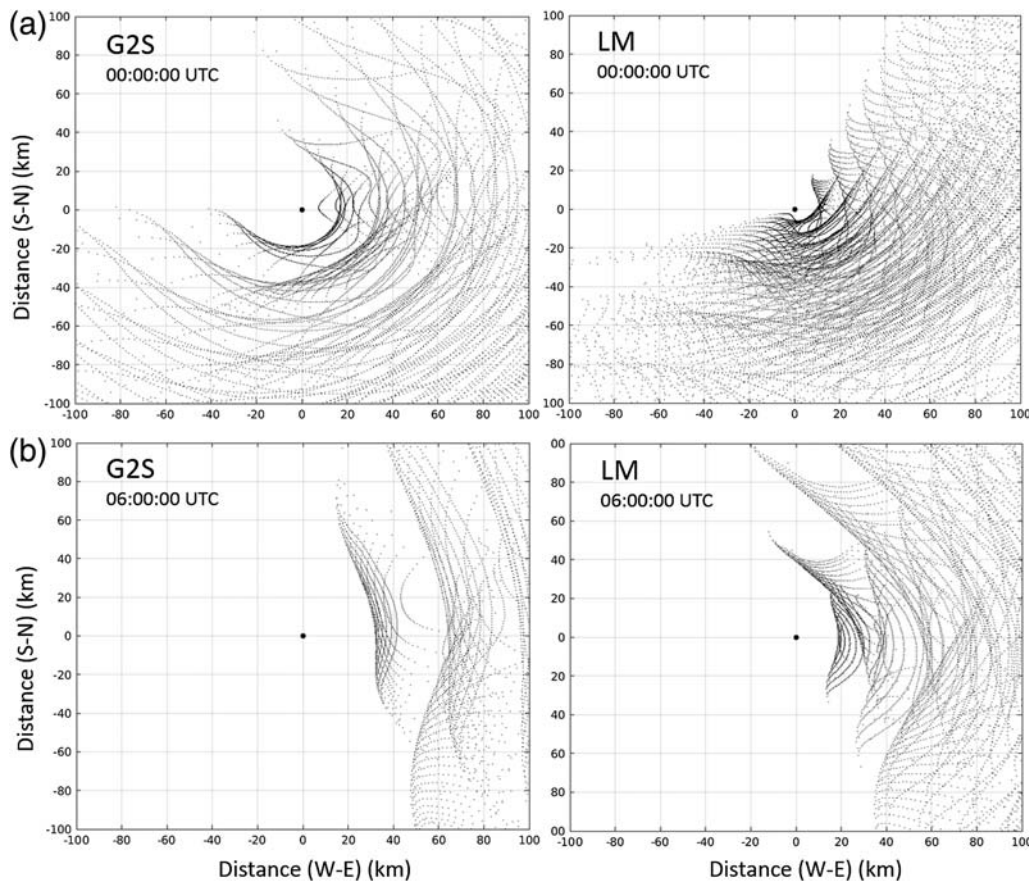


**Figure 10.** Raytracing results using the tropospheric models based upon G2S specifications (left) and LM data (right) for 2 January 2012 at (a) 00:00:00 and (b) 06:00:00 UTC.

human detections is dependent on the rms amplitude that is correlated with wind velocity. The number of analysts' detections in all cases is the largest for average rms amplitudes between 1.2 and 3.2 MPa and includes most of the signals detected by the automated procedures (Fig. 11b). Most analysts identified signals under higher noise conditions, although the largest number of detections identified by the analysts occurred during noise conditions with average rms amplitudes below 3.2 MPa. When the large aperture arrays were used in AFD and PMCC, significantly lower numbers of detections were identified during time periods of higher average rms amplitudes. Figure 11c illustrates the relationship between the SNR and the number of detections for both the automatic and manual detectors, with the step in number of detections reflective of SNR increases. PMCC has a significantly larger number of detections when the small aperture arrays are used under high-SNR conditions.

### Discussion

This work documents the characteristics of two automatic detectors under different input parameters and different array configurations with varying noise conditions and compares their performance against analysts' picks. EROC introduced in this study provides an empirical procedure for

assessing array performance using observational data but suffers from the possibility that all the signals in the dataset may not be labeled. The result, though, provides a basis for quantifying the effects of array configuration and time-varying noise conditions on performance, as well as insight into how to optimally operate automated detectors.

Both detectors perform poorly for high frequencies (1–5 Hz) when large array apertures ( $\sim 1$  km) were used. Generally, the small array aperture ( $< 100$  m) for PMCC and small plus large aperture arrays and all array elements for AFD are recommended for high-frequency signal analysis under both low- and high-noise conditions. AFD can be tuned using the  $p$ -value to reduce the false detections under high-noise conditions.

Possible sources of the signals were characterized based on raytracing, using both global and LM data. CHNAR is ensonified by tropospheric returns at relatively short distances ( $< 200$  km) for the time period explored in this study, consistent with detections from the west and northwest of the array. A second set of detections from the east and southeast are possibly related to near-surface winds and a possible inversion layer. These azimuths are also consistent with some very close-by seismic events within 12–35 km of the array, suggesting that these signals are very local and might be considered clutter for regional studies. McKenna *et al.* (2008)

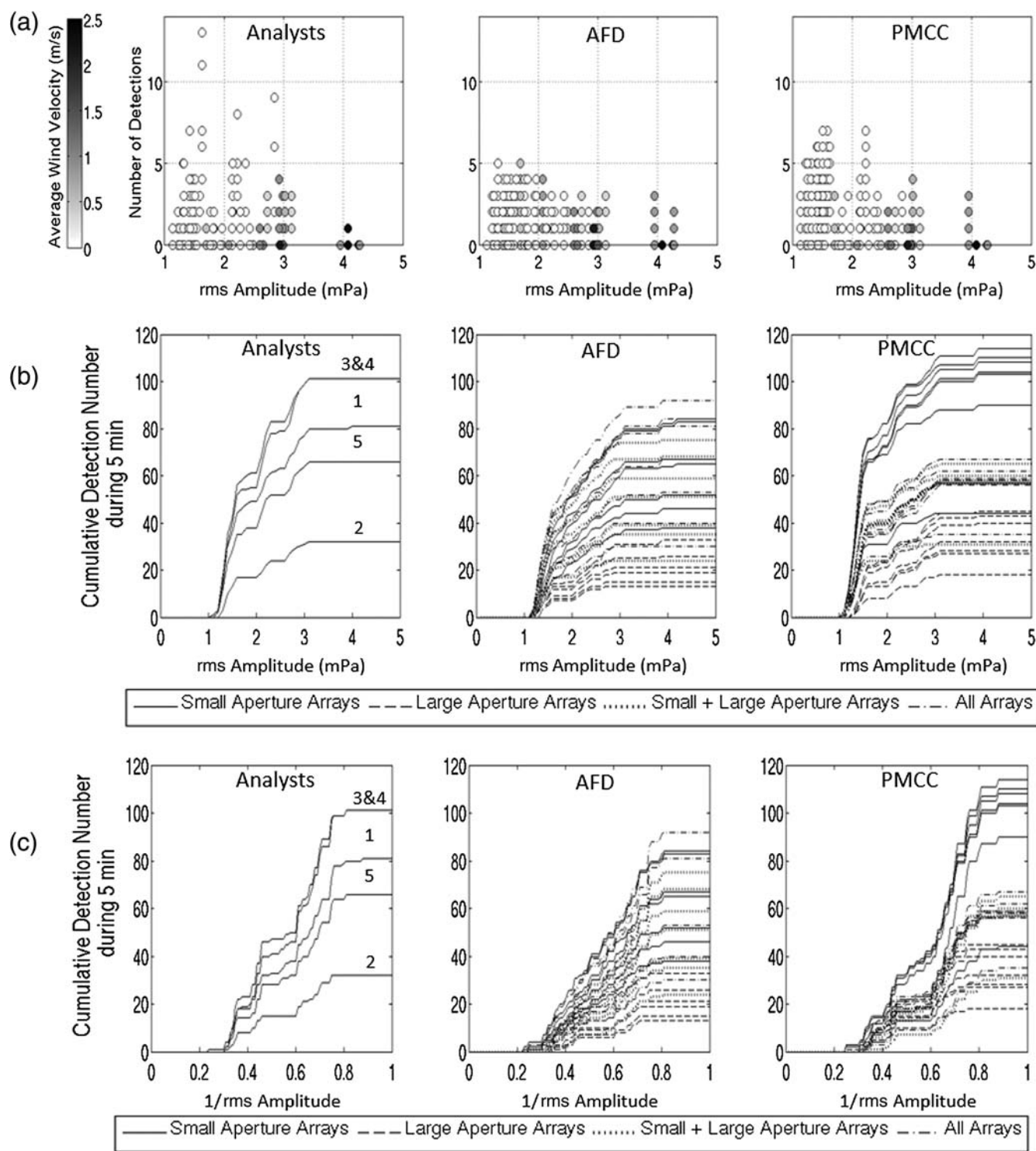


**Figure 11.** (a) Relationship between the number of detections estimated by the automated analysis and the analyst review during consecutive 5-min windows compared with wind velocity and average rms amplitude. The cumulative number of detections in all the 5-min windows for the analysts and the automatic detectors using different array configuration are plotted against (b) the average rms amplitude in the window and (c)  $1/\text{average rms amplitude}$  that is proportional to the signal-to-noise ratio.

documented that large numbers of infrasound arrivals are recorded at CHNAR during working times and that some arrivals may not be cataloged. They suggested lonesome infrasound arrivals needed analyst review and hypothesized

that the majority of these arrivals are associated with low-atmosphere ephemeral ducts. Park *et al.* (2016) document that infrasound detections at this site are affected by tropospheric wind during the wintertime based on the analysis of

1 year of data. Other studies ([Che et al., 2002](#); [Stump et al., 2004](#); [McKenna et al., 2008](#)) concluded that LM data better predicted infrasound arrivals over short distances than global-scale atmospheric models such as MSISE (Mass Spectrometer Incoherent Scatter Extension 1990), HWM (Horizontal Wind Model 1993), and G2S. Even though the LM observatory is about 100 km from CHNAR, it provides ray predictions on a fine scale that are consistent with some of the lonesome infrasound observations. These results suggest that it is critical to understand both fine- and medium-scale characteristics of the atmosphere to fully assess array performance. Additionally, they illustrate the importance of establishing event ground truth in assessing detector performance and associated tuning.

This focused study motivates the exploration of the automated detectors using datasets covering longer time periods, additional arrays, as well as broader environmental conditions to illuminate the impact of noise and geographic environments on optimizing automated detections as well as characterization of performance. Extension to regional networks of infrasound arrays using the same sources will provide the capability to assess network performance, including signal association and subsequent location across the area covered by the network.

## Conclusions

The performance of two automatic detectors (AFD and PMCC) was evaluated and compared with picks by five analysts. A 4-hr time sample at the array CHNAR located in South Korea was used with  $\sim 2$  hrs of low wind velocity and noise and 2 hrs of increased wind and noise. Automatic detections are dependent on tuning parameters specific to each procedure as well as background noise level. Several tuning parameters that depend on the character of the anticipated signals are common to the two detectors, including the window length of 20 s, overlap of 50%, and a filter band from 1 to 5 Hz based on the focus on regional infrasonic signals. In the case of PMCC, the standard deviation of  $10^\circ$  for azimuth and 20 m/s for phase velocity with a range from 200 to 450 m/s were used for grouping detections into families. For AFD, the adaptive window of 1 hr was used, and the ranges of phase velocity and azimuth were unconstrained. Detection performance tests for both detectors were conducted with respect to different values of consistency for PMCC and  $p$ -value for AFD, as well as different array configurations (small, large, small + large aperture arrays, and all array elements).

## Summary of Study Results

- Five analysts, each with their own detection criteria, reviewed the 4-hr dataset, and their detections were used to assess the automated detectors. During high-noise conditions, analysts reported difficulty in identifying signals, with the possibility that a number of signals went undetected or in some cases were identified as coherent noise across the array.

- Detection performance for both manual and automatic (PMCC and AFD) picks depends on noise level that changes as a function of time: higher surface wind velocities produce increased rms amplitudes. Surface wind speed and possibly direction measured at the array can be used not only to assess changing noise environments but also to infer local detection capabilities at an array. In this work, adaptive noise processing by AFD is affected by weather conditions, as illustrated by the time-varying  $C$ -value. This adaptation depends on the array aperture, with larger  $C$ -value variations for smaller array apertures, indicating higher sensitivity to noise levels on the small aperture array configurations.
- The two detectors were tested using four different starting configurations or subnetworks. PMCC produces a more conservative estimate of detections using a single subnetwork compared with estimates using multiple subnetworks. Both detectors were tested with a range of detection thresholds (consistency value for PMCC and  $p$ -value for AFD). For each detector, the number of detections increased with an increase in detection threshold. Utilization of only the large aperture array ( $\sim 1$  km) produced the smallest number of detections. Detections produced by PMCC were more dependent on array configuration, with the most detections estimated using the small aperture arrays ( $\sim 100$  m).
- EROC analysis was proposed and implemented. The new procedure uses common readings from the analysts to identify detections for an alternative performance assessment.
  1. Under low-noise conditions (first 2 hrs of data), the two automated detectors produce similar detection trends, with the highest  $P_d$  for PMCC of  $\sim 0.62$  using small aperture arrays and a  $P_d$  for AFD of  $\sim 0.59$  using all array elements. When using small plus large aperture arrays or all array elements,  $P_d$  from AFD for all  $p$ -values are larger than those from PMCC.  $P_d$  and  $P_f$  for PMCC do not vary much with consistency values, except in the case in which the large aperture array is used. Both detectors' performances degrade using only the large aperture array.
  2. PMCC and AFD perform differently under high-noise conditions (last 2 hrs of data). Both detectors produce a higher  $P_d$  ( $\sim 0.69$  for PMCC and  $\sim 0.64$  for AFD) using small aperture arrays. AFD has a broader range and higher absolute value of  $P_f$  (0.01–0.34) compared to PMCC (0.01–0.08). This empirical study suggests that PMCC performs closer to the analysts in which the smaller aperture arrays increased the  $P_d$ . In the case of AFD, smaller  $p$ -values are recommended to minimize  $P_f$ .
- $P_d$  values from the automatic detectors are impacted most by noise level, with low noise (average rms amplitude of 1.7 MPa) having an average  $P_d$  of  $\sim 0.42$  (all

detector tests) and an average  $P_f$  of  $\sim 0.10$  and high noise (average rms amplitude of 2.9 MPa) having an average  $P_d$  of  $\sim 0.30$ , with an average  $P_f$  of  $\sim 0.08$ . Generally, the number of analysts' detections is the greatest for average rms amplitudes between 1.2 and 3.2 MPa, including most of the detections estimated by the automated procedures.

- In most cases, the larger array dimensions on the order of 1 km performed worse for 1–5 Hz signals than the small array configuration ( $\sim 100$  m) or some combination of small and large array elements. Signal correlation decreases for the larger offsets that may reflect contributions from signals generated at local distance near the array, rather than regional distances.
- Many detections identified by the automated detectors and analysts are from  $90^\circ$  to  $210^\circ$  and from  $240^\circ$  to  $330^\circ$  during the 4-hr time period, possibly linked to man-made sources documented in previous studies (Che *et al.*, 2002; Stump *et al.*, 2004; McKenna *et al.*, 2008). Phase velocities are relatively fast (320–350 m/s), indicative of a combination of near-surface and tropospheric arrivals. Based on the raytracing, detections from  $300^\circ$  to  $330^\circ$  are associated with dominant tropospheric winds at the time of the observations. The tropospheric model using LM data has a finer-scale bounce distance ( $\sim 5$  km from the source) in the ensonified region than those ( $\sim 20$  km) from G2S atmospheric data, suggesting that tropospheric arrivals from short distances can be observed at CHNAR during the wintertime (Park *et al.*, 2016).
- The large number of detections from  $90^\circ$  to  $210^\circ$ , especially during low-noise conditions, is not consistent with the tropospheric models. Near-surface winds recorded at CHNAR during the first 2 hrs of the data are from the south and east, consistent with the azimuth of the detections. The fact that the seismic signals during the same time period are associated with these azimuths and from within kilometers of the array suggests that these signals may be dominated by the fine details in the near-surface atmosphere, including surface winds and the possibility of a wintertime inversion layer near the array. These nearby sources might be considered clutter in the context of detecting and locating the source of regional infrasound signals.

## Data and Resources

Southern Methodist University (SMU) and Korea Institute of Geoscience and Mineral Resources (KIGAM) collected the infrasound data used in this study, and data used in this study are available through the authors upon request.

## Acknowledgments

The Air Force Research Laboratory, under Award Number FA8718-08-C-0008, funded this work. We would like to thank Yves Cansi of Commissariat à l'Energie Atomique (CEA) and Il-Young Che of Korea Institute of Geoscience and Mineral Resources (KIGAM) for their helpful comments

for the initial assessment of progressive multichannel correlation (PMCC). We also thank Alexis Le Pichon of CEA and Maurice Charbit of Institut Mines-Télécom for their valuable comments that improved our article. We thank Mason MacPhail and Petru Negruț of Southern Methodist University (SMU) for volunteering the analyst review work. We acknowledge Douglas Drob at Naval Research Laboratory (NRL) for providing the Ground-to-Space (G2S) atmospheric specifications. The MERRA/GEOS-5 data utilized in the G2S atmospheric specifications were provided by the Global Modeling and Assimilation Office (GMAO) at National Aeronautics and Space Administration (NASA) Goddard Space Flight Center through the online data portal in the NASA Center for Climate Simulation. The National Oceanic and Atmospheric Administration (NOAA) Global Forecast System (GFS) analysis fields, also utilized in the G2S specifications, were obtained from NOAA's National Operational Model Archive and Distribution System (NOMADS), which is maintained at NOAA's National Climatic Data Center (NCDC). We are grateful for important comments and suggestions made by Associate Editor Eric Chael and the three anonymous reviewers.

## References

- Arrowsmith, S. J., C. Hayward, B. Stump, R. Burlac, I.-Y. Che, and G. Singh (2008). Multi-array detection, association and location of infrasound and seismo-acoustic events in Utah, *Proc. of the 2008 Monitoring Research Review: Ground-Based Nuclear Explosion Monitoring Technologies, LA-UR-08-05261*, Vol. 2, 844–852.
- Arrowsmith, S. J., R. Whitaker, C. Katz, and C. Hayward (2009). The F-detector revisited: An improved strategy for signal detection at seismic and infrasound arrays, *Bull. Seismol. Soc. Am.* **99**, 449–453.
- Blandford, R. R. (1974). An automatic event detector at the Tonto Forest seismic observatory, *Geophysics* **39**, 633–643.
- Blandford, R. R. (2002). Detection and azimuth estimation by infrasonic arrays as a function of array aperture and signal coherence, *Technical Rept. AFTAC-TR-02*, 10–13.
- Blom, P., and R. Waxler (2012). Impulse propagation in the nocturnal boundary layer: Analysis of the geometric component, *J. Acoust. Soc. Am.* **131**, 3680–3690.
- Brown, D. J., B. L. N. Kennett, and C. Tarlowski (2002). Infrasound signal detection via the Hough transform, *Infrasound Technology Workshop 2002*, Royal Netherlands Meteorological Institute (KNMI), De Bilt, The Netherlands.
- Brown, D. J., R. Whitaker, B. L. N. Kennett, and C. Tarlowski (2008). Automatic infrasonic signal detection using the Hough transform, *J. Geophys. Res.* **113**, D17105, doi: [10.1029/2008JD009822](https://doi.org/10.1029/2008JD009822).
- Cansi, Y. (1995). An automated seismic event processing for detection and location: The P.M.C.C. method, *Geophys. Res. Lett.* **22**, 1021–1024.
- Cansi, Y., and A. Le Pichon (2009). Infrasound event detection using the progressive multi-channel correlation algorithm, in *Handbook of Signal Processing in Acoustics*, D. Havelock, S. Kuwano, and M. Vorländer (Editors), Springer, New York, New York, 1425–1435.
- Che, I.-Y., M.-S. Jun, J.-S. Jeon, and K. D. Min (2002). Analysis of local seismo-acoustic events in the Korean Peninsula, *Geophys. Res. Lett.* **29**, 1589, doi: [10.1029/2001GL014060](https://doi.org/10.1029/2001GL014060).
- Christie, D. R., and P. Campus (2010). The IMS infrasound network: Design and establishment of infrasound stations, in *Infrasound Monitoring for Atmospheric Studies* A. Le Pichon, E. Blanc, and A. Hauchecorne (Editors), Springer, New York, New York, 29–75.
- Coyne, J., and I. Henson (1995). Geotool sourcebook: User's manual, Teledyne Brown Engineering, *Scientific Rept. No. 1 PL-TR-96-2021*.
- Drob, D. P., J. M. Picone, and M. Garces (2003). Global morphology of infrasound propagation, *J. Geophys. Res.* **108**, 4680, doi: [10.1029/2002jd003307](https://doi.org/10.1029/2002jd003307).
- Evers, L. G., and H. W. Haak (2001). Listening to sounds from an exploding meteor and oceanic waves, *Geophys. Res. Lett.* **28**, 41–44, doi: [10.1029/2000GL011859](https://doi.org/10.1029/2000GL011859).
- Freedman, H. W. (1966). The “little variable factor” a statistical discussion of the reading of seismograms, *Bull. Seismol. Soc. Am.* **56**, 593–604.

- Garcés, M., and C. Hetzer (2002). Evaluation of infrasonic detection algorithms, *Proc. of the 24th Seismic Research Review—Nuclear Explosion Monitoring: Innovation and Integration, LA-UR-02-5048*, Vol. 2, 745–754.
- Hagerty, M. T., W.-Y. Kim, and P. Martysevich (1999). Characteristics of infrasound produced by large mining explosions in Kazakhstan, *Proc. of the 21st Annual Seismic Research Symposium on Monitoring a Comprehensive Nuclear-Test-Ban Treaty*, 123–132.
- Hart, D. (2004). Automated infrasound signal detection algorithms implemented in MatSeis—Infra tool, *Sandia Rept. SAND2004-1889*.
- Hedlin, M. A. H., C. de Groot-Hedlin, and D. Drob (2012). A study of infrasound propagation using dense seismic network recordings of surface explosions, *Bull. Seismol. Soc. Am.* **102**, 1927–1937, doi: [10.1785/0120110300](https://doi.org/10.1785/0120110300).
- Johnson, D. H., and D. E. Dudgeon (1993). *Array Signal Processing: Concepts and Techniques*, A. V. Oppenheim (Series Editor), Prentice Hall, Upper Saddle River, New Jersey, 213–215.
- Kalnay, E., M. Kanamitsu, and W. Baker (1990). Global numerical weather prediction at the National Meteorological Center, *Bull. Am. Meteorol. Soc.* **71**, 1410–1428.
- Kay, S. (1998). *Fundamentals of Statistical Signal Processing: Detection Theory*, Chapter 3, Vol. II, Prentice Hall, Englewood Cliffs, New Jersey.
- Leonard, M. (2000). Comparison of manual and automatic onset time picking, *Bull. Seismol. Soc. Am.* **90**, 1384–1390.
- Matoza, R. S., M. Landès, A. Le Pichon, L. Ceranna, and D. Brown (2013). Coherent ambient infrasound recorded by the International Monitoring System, *Geophys. Res. Lett.* **40**, doi: [10.1029/2012GL054329](https://doi.org/10.1029/2012GL054329).
- McKenna, M. H., B. W. Stump, and C. Hayward (2008). Effect of time-varying tropospheric models on near-regional and regional infrasound propagation as constrained by observational data, *J. Geophys. Res.* **113**, D11111, doi: [10.1029/2007JD009130](https://doi.org/10.1029/2007JD009130).
- Park, J. (2013). *Infrasound Signal Processing from Regional Arrays and Seismic Characteristics of North Korean Nuclear Explosions*, Ph.D. Thesis, Southern Methodist University, Dallas, Texas, 27–36.
- Park, J., B. W. Stump, C. Hayward, S. J. Arrowsmith, I.-Y. Che, and D. P. Drob (2016). Detection of regional infrasound signals using array data: Testing, tuning, and physical interpretation, *J. Acoust. Soc. Am.* **140**, no. 1 239–259.
- Rost, S., and C. Thomas (2002). Array seismology: methods and applications, *Rev. Geophys.* **40**, doi: [10.1029/2000RG000100](https://doi.org/10.1029/2000RG000100).
- Sereno, T. J. (1990). *Attenuation of Regional Phases in Fennoscandia, and Estimates of Arrival Time and Azimuth Uncertainty using Data Recorded by Regional Arrays*, SAIC-90/1472, Science Applications International Corp., San Diego, California.
- Shumway, R. H., S. Kim, and R. R. Blandford (1999). Nonlinear estimation for time series observed on arrays, in *Asymptotics, Nonparametrics, and Time Series*, S. Ghosh (Editor), Marcel Dekker, New York, New York, 227–258.
- Sipkin, S. A., W. J. Person, and B. W. Presgrave (2000). Earthquake bulletins and catalogs at the USGS National Earthquake Information Center, *Incorporate Research Institutions for Seismology Newsletter 2000*, Vol. 1, 2–4.
- Stump, B., M.-S. Jun, C. Hayward, J.-S. Jeon, I.-Y. Che, K. Thomason, S. M. House, and J. McKenna (2004). Small-aperture seismo-acoustic arrays: Design, implementation, and utilization, *Bull. Seismol. Soc. Am.* **94**, 220–236.
- Vernon, F., J. Tytell, B. Busby, J. Eakins, M. Hedlin, A. Muschinski, K. Walker, and B. Woodward (2012). Scientific viability of the USAArray transportable array network as a real-time weather monitoring platform, presented at the *92nd American Meteorological Society Annual Meeting*, New Orleans, Louisiana, 24 January 2012.
- Zeiler, C. P., and A. A. Velasco (2009). Seismogram picking error from analyst review (SPEAR): Single-analyst and institution analysis, *Bull. Seismol. Soc. Am.* **99**, 2759–2770.

Roy M. Huffington Department of Earth Sciences  
 Southern Methodist University  
 3225 Daniel Avenue  
 Dallas, Texas 75205  
 junghyunp@smu.edu  
 (J.P., C.T.H., B.W.S.)

Pinedale Seismic Research Facility  
 635 Highway 353  
 Boulder, Wyoming 82923  
 (C.P.Z.)

Sandia National Laboratories  
 1515 Eubank Boulevard  
 Albuquerque, New Mexico 87123  
 (S.J.A.)

Manuscript received 27 April 2016;  
 Published Online 31 January 2017